JPhys Photonics

PAPER • OPEN ACCESS

Defect-free laser powder bed fusion of Ti–48Al–2Cr–2Nb with a high temperature inductive preheating system

JPhys Photonics

PAPER

Defect-free laser powder bed fusion of Ti–48Al–2Cr–2Nb with a high temperature inductive preheating system

Leonardo Caprio[1], **Ali Gökhan Demir**, **Gianmarco Chiari** and **Barbara Previtali**

Department of Mechanical Engineering, Politecnico di Milano, Via La Masa 1, I-20156, Milano, Italy
[1] Author to whom any correspondence should be addressed.

E-mail: leonardo.caprio@polimi.it, aligokhan.demir@polimi.it, gianmarco.chiari@mail.polimi.it and barbara.previtali@polimi.it

Keywords: high temperature, laser powder bed fusion, preheating, TiAl, energy generation, additive manufacturing

OPEN ACCESS

RECEIVED
7 August 2019

REVISED
10 December 2019

ACCEPTED FOR PUBLICATION
27 January 2020

PUBLISHED
12 February 2020

Abstract

In the industrial panorama, laser powder bed fusion (LPBF) systems enable the near net shaping of metal powders into complex geometries with unique design features. This makes the technology appealing for many industrial applications, which require high performance materials combined with lightweight design, lattice structures and organic forms. However, many of the alloys that would be ideal for the realisation of these functional components are classified as difficult to weld due to their cracking sensitivity. γ-TiAl alloys are currently processed via electron beam melting (EBM) to produce components for energy generation applications. The EBM process provides crack-free processing thanks to the preheating stages between layers, but lacks geometrical precision. The use of LPBF could provide the means for higher precision, and therefore an easier post-processing stage. However, industrial LPBF systems employ resistive heating elements underneath the base plate which do not commonly reach the high temperatures required for the processing of γ-TiAl alloys. Thus, elevated temperature preheating of the build part and control over the cooling rate after the deposition process is concluded are amongst the features which require further investigations. In this work, the design and implementation of a novel inductive high temperature LPBF system to process Ti–48Al–2Cr–2Nb is presented. Specimens were built with preheating at 800 °C and the cooling rate at the end of the build was controlled at 5 °C min^{-1}. Crack formation was suppressed and apparent density in excess of 99% was achieved.

1. Introduction

Laser powder bed fusion (LPBF), also known as selective laser melting (SLM), employs a highly energetic laser beam to selectively deposit a layer of metallic powder feedstock upon a substrate material. The process is thus repeated layer-by-layer as typically done in other additive manufacturing (AM) processes. In order to obtain stable processing conditions and high part density, full melting of the powder bed is required. Hence, for the processing of metallic powders, LPBF requires the use of a beam with elevated energy density which has been enabled by the development of high brilliance fiber laser sources in recent years [1]. Although, the LPBF technology has been witnessing an increasing interest on behalf of the industrial world, its applicability is mainly restricted to the processing of weldable alloys. The main reason behind the limitation in the range of processable materials is linked to the elevated thermal gradients and cooling rates that are experienced locally during the fusion process and are intrinsic to the technology due to the concentrated energy beam required to melt the powder bed. Cooling velocities greater than 10^6 K s^{-1} have been measured experimentally by Scipioni *et al* [2] while Shi *et al* estimate thermal gradients above 10^4 K mm^{-1} [3]. As clearly explained by Hagedorn *et al* these values are critical when processing metallic powders due to the elevated stress concentrations which are generated [4].

Powder bed preheating has thus been extensively employed since the onset of the LPBF technology [5]. Initially, its role was of lowering the energy density required to achieve full melting of the feedstock material but,

with the introduction of high brilliance fiber lasers, the main scope became the minimisation of thermal tensions which form locally. As a matter of fact, all of the industrial systems are equipped with preheating systems allowing the reduction of thermal stresses in the first layers of the building process. In the initial depositions of the AM process, the reduction of thermal stresses is essential due to the presence of the substrate base which acts as a heat sink and thus causes the formation of even higher thermal gradients and cooling rates.

Different techniques of substrate preheating have been applied to the LPBF technology, namely IR heaters [5–7], preheating or remelting strategies through fast scanning of the laser beam [8–10], use of a second defocused laser beam [11], substrate resistive heating [12, 13] or baseplate induction circuit [4, 14, 15]. The greater part of industrial SLM systems employs resistive heaters, which typically allow preheating of the baseplate up to 200 °C while the most recently developed systems enable to achieve up to 800 °C [13]. Although these systems are particularly effective in reducing local stresses near the base plate, they lose their effectiveness when a full-scale component must be manufactured since their area of influence is limited to the lower parts of the build (due to the inherent nature of the process which relies on the lowering of the base plate). A similar preheating concept was developed by Hagedorn *et al* whom employed a pancake induction heating circuit capable of achieving up to 1000 °C [14, 15]. IR heaters have been applied for the preheating of the top layer of the powder bed, however these systems are not energetically efficient [5, 7]. In general, the use of high temperature preheating systems can also provide the means to a higher productivity enabled by the added energy to the process and improved optical absorptivity at higher temperatures, as well as reducing the residual stresses [16].

Alternatively, the use of a second defocused laser beam may be effective in reducing residual stresses as estimated by Aggarangsi *et al* [17] and demonstrated experimentally by Wilkes *et al* [11]. Although this approach is effective when processing non-metallic materials, it implies a higher capital cost of the AM machine since a second optical set-up and laser source must be equipped for this solution. Preheating or remelting strategies employing the same process laser can be effective in reducing porosity as demonstrated by Demir *et al* [9, 10] and Aboulkhair *et al* [8]. However, these imply a notable increase in terms of production time due to the double scanning of the powder bed required. A competing technology which relies on a similar preheating concept is electron beam melting (EBM). This technology is capable of achieving powder bed temperatures in the order of 1000 °C thanks to preheating scans applied prior to the melting stage which are enabled by the fast magnetic coil deflection system [18].

Taking into consideration the available technologies and the need for uniform high preheating temperatures for the processing of crack susceptible alloys, the aim of the present work was the development of a novel high temperature laser powder bed fusion (HT-LPBF) system, namely project *Grisù* [19]. The system was studied in order to additively manufacture γ-TiAl alloys using a high power laser beam even though this type of material is generally prone to cracking due to the elevated temperature gradients and cooling rates involved in the process. γ-TiAl alloys are used in the energy industries since they are characterized by resistance to high temperatures and oxidation with low density [20]. The γ-TiAl alloys are commonly processed by EBM technology to produce turbine blades with complex geometries and improved thermal performance. However, a downside of the EBM process is that the minimum feature achievable and overall geometrical precision are limited by the melt pool dimension which is typically greater in comparison to LPBF systems [18, 21, 22]. The lack of geometrical precision requires larger machining allowances and the post-processing stage becomes very complicated due to the complex geometry of the product. LPBF can potentially provide a higher geometrical precision due to the smaller beam size and reduce the post-processing burden. However, the ductile-brittle transition of the alloy (which tends to occur around 750 °C) makes the production route involving LPBF even more challenging, as observed by Vilaro *et al* [23]. In the current literature, Löber *et al* have witnessed the presence of cracking already during single track deposition of a γ-TiAl alloy [24]. Similarly, Doubenskaia *et al* with a preheating up to 450 °C witnessed cracks during the realisation of cubic specimen of Ti–48Al–2Cr–2Nb [25].

The majority of research regarding γ-TiAl deposited by means of LPBF concentrates on the material properties (as demonstrated by the various publications by the research group from the Huazhong University of Science and Technology [26–29] and the work by Chenglong *et al* [30]). Still, these analyses are conducted without having optimised the processing conditions to achieve part relative densities in excess of 99%. Thus, technological challenges which allow to achieve high density specimen without the presence of cracks or other defects should initially be addressed.

In the present research, a preheating system was incorporated in a LPBF machine with a different geometry with respect to that implemented by Hagedorn *et al* [4]. The EBM technology or IR heating systems are capable of heating the last few layers of the powder bed. On the other hand, baseplate inductive or resistive heating systems are effective only for low build heights. The solution developed in the current research enables a constant preheating throughout the whole build process. Instead of employing a pancake coil, the novel HT-LPBF was designed with a helical coil which contains the substrate base as it is lowered during the building process. Other than providing high preheating temperatures, the systems maintains the preheating temperature constant throughout the build, as well as controlling the cooling rate at the end of the process. Hence, the use of

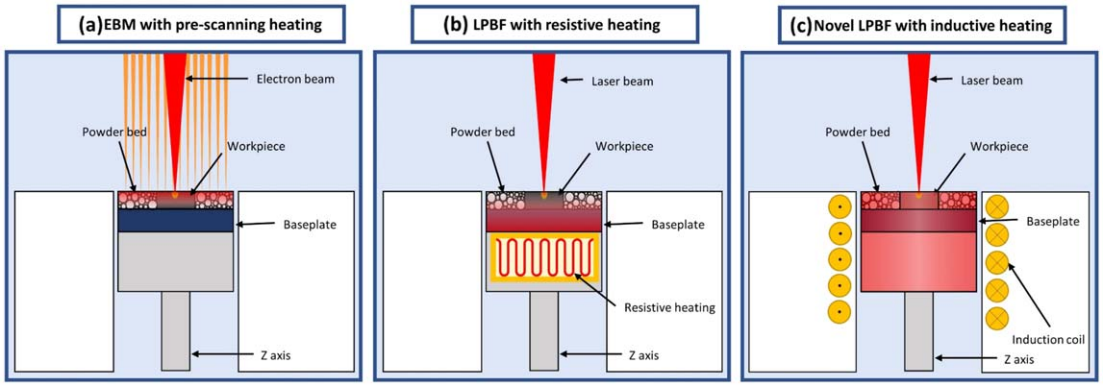

Figure 1. Conceptual layout design of (a) EBM with pre-scanning heating (b) LPBF with standard resistive preheating system and (c) novel LPBF with inductive heating system.

this innovative system architecture might not only open the road for the processing of crack susceptible alloys but also for the realisation of *in situ* heat treatments during the freeform fabrication process.

The scope of this article is to present this new conceptual AM system and is structured as follows: the design of project *Grisù* is presented and the testing of the induction system to achieve preheating temperatures above 800 °C is reported, where the preheating temperature was maintained constant throughout the build and a controlled cooling rate at the end of the build process was employed. Eventually a demonstrator build using a γ-TiAl alloy prone to crack formation is realised with and without the use of the preheating system. Results show that the prototypal system is effective in suppressing crack formation and acts as proof of concept of the novel HT-LPBF system architecture.

2. Materials and methods

2.1. Design of the inductive preheating system

Project *Grisù* was born with the aim of developing an innovative AM system whilst keeping the advantages of an open-ended laboratory set-up. For this reason, the prototypal system was designed to operate with low quantities of powder, similarly to its predecessor, project *Powderful* [31]. The novel conceptual design of the preheating system is compared to the classical resistive baseplate and EBM technology in the schematic representation of figure 1.

A critical aspect of the design of the prototype was the choice of materials for the different components. It was essential that the most stressed components of the system could sustain temperatures up to 800 °C whilst not being influenced by the strong magnetic field generated by the induction coil. For this reason, quartz glass was selected for the cylinder containing the movable part of the *z*-axis. The piston was realised in *Cerastil* (Formenti, Milano, Italy) a poly-silicate material capable of withstanding up to 1100 °C. Accordingly, the gasket of the piston which prevents powder infiltration in the *z*-axis was realised in *Paperseal* (Formenti, Milano, Italy) a mineral fibre material. The fixed plane of the powder bed was designed to be in ceramic glass whilst the helical coil for the preheating system was of pure copper.

A small steel cylinder was located within the piston which inductively heats up during the printing process and contributes to preheating the metallic substrate by means of conduction. Considering that the prototypal system may be employed to study the processing of non-metallic materials, which must thus be deposited upon non-metallic substrates, the steel cylinder will act as the heat source for the preheating system. In the present work, for the testing of the preheating system of project *Grisù* Ti6Al4V was chosen as substrate material. Titanium alloys, although they are light and non-ferrous materials, tend to behave similarly to steel when heated inductively (since they possess analogous values of electrical resistivity and thermal conductivity) [32]. Hence, the whole substrate base can be expected to be effectively heated up by means of the inductive preheating system. On the other hand, during the printing process the induction field will also have an influence over the powder bed. Although, the effect in terms of inductive preheating on metallic powders is unclear in literature and will be the focus of future studies, the system will still be effective in preheating the solidly deposited material.

The heart of project *Grisù* was designed with three water heat exchangers in order to contain the elevated temperatures generated by the induction heating system. An adequate cooling system is fundamental to avoid distortions of other mechanical parts and in particular to guarantee the accuracy of the *z*-axis movement system.

#	Component	Material	T_{max} (°C)
1	Piston	Cemestil	1100
2	Gasket	Paperseal	1100
3	Plane	Ceramic glass	800
4	Cylinder	Quartx glass	1250
5	Induction coil	Pure Cu	250
6	Fixed heat exchanger	Al-alloy	400
7	Moving heat exchanger	Al-alloy	400
8-9	Nut and screw	Carbon steel	500
10	Piston-Heat exchanger connection	Carbon steel	500
11	Rebored bar	Carbon steel	500
12	Linear bearing	Steel	500
13	Motor transmission	Elastomer	70
14	Stepper motor	Mixed	70
15	Steel insert	Carbon steel	1000
16	Thermocouple position		

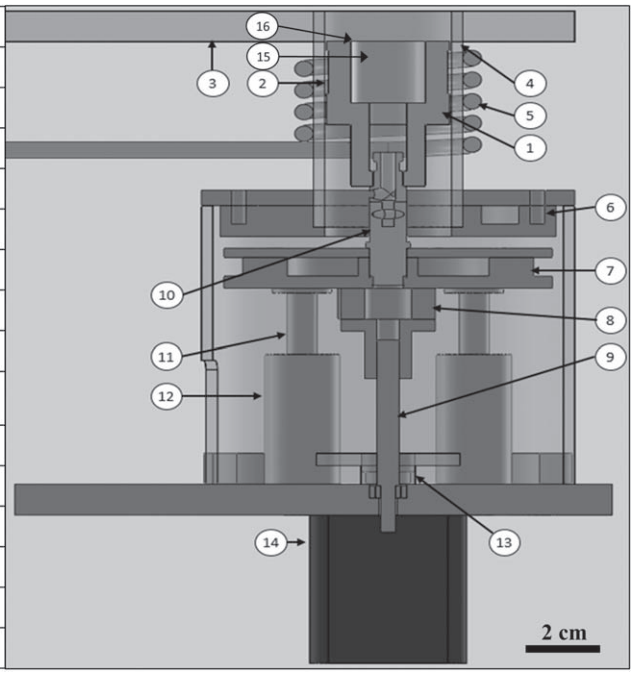

Figure 2. List of materials, their maximum operational temperature T_{max} and design of the preheating system.

The first heat exchanger is the induction coil itself which is composed of copper tubes where water is forced to flow. This acts not only as a barrier for the heat flow with respect to the rest of the machine but also plays an important role in maintaining the copper tubes cooled. A second flat water-cooled heat exchanger is located in a fixed position beneath the heart of the induction system. The third water-cooled component translates along the z-axis as it is lowered during the build job and is responsible of maintaining at a low temperature the motor transmission. Temperature sensors were placed on these components in order to monitor their temperature and avoid them from achieving excessive values. The components and their respective materials are listed in figure 2, alongside with a side view of the design of the preheating system and z-axis. T_{max} refers to the maximum operational temperature of the different components (depending on their material). These were indicated within the specifications given by the part producers and suppliers. Although, relatively high values of T_{max} are indicated for the mechanical components the heat exchangers design is supposed to maintain these values below 100 °C.

The final design and realisation of project *Grisù* is shown in figure 3. The recoater blade was realised in stainless steel in order to withstand the elevated temperatures of the powder bed. The system is equipped also with a fan which provides a gas flow above the build area. The whole prototypal system can be placed within an inert gas chamber (analogously to the previous prototypal system developed [31]). Before each build and the activation of the preheating system, an inertization procedure of the closed chamber was conducted, applying a vacuum down to 50 mBar and then filling the process chamber with high purity Ar gas. The whole mechanical control of the system is conducted with a self-developed LabVIEW code (National Instruments, Austin, TX, USA).

2.2. Laser optical delivery system

For the present research, a 1000 W single-mode fibre laser source (n-Light, Vancouver, WA, USA) was employed as the light source. The beam path was controlled with a Smart Scan SH30G-XY2 scanner head (Smart Move GmbH, Garching bei München, Germany), whereby the laser emission was collimated with a 75 mm lens and focused onto the substrate using a 420 mm F-theta lens. The beam diameter on the focal plane was determined from theoretical calculations as $d_0 = 78\ \mu$m. Scan path trajectories could be flexibly designed by use of the Scan Master Designer software (Cambridge Technologies, Bedford, MA). Overall, the principal features of project *Grisù* are reported in table 1.

In order to verify the functionality of the high temperature preheating system, a measurement chain to keep track of the temperature variations within the powder bed was designed and implemented. A K-type thermocouple was employed for this scope (TERSID, Milano, Italy) which is indicated for use in these

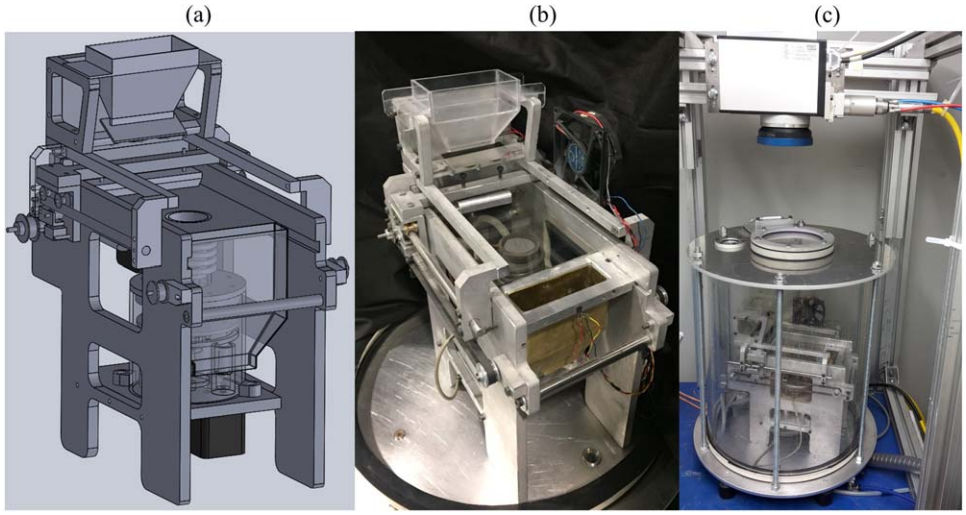

Figure 3. Project *Grisù* (a) CAD design (b) assembled prototype system (c) final set-up.

Table 1. Characteristics of project *Grisù*, the HT-LPBF system.

Parameter	Value
Laser source	n-Light Alta Prime
Laser max. power, P_{max}	1 kW
Beam quality factor, M^2	1.19
Max. scan speed, $v_{scan,\ max}$	5 m s^{-1}
Spot diameter, d_0	78 μm
Layer thickness, z	30–100 μm
Process atmosphere	Ar; N_2
Build plate diameter, ϕ	38 mm

processing conditions by the producer. The measurement point was selected just beneath the substrate position such that the actual temperature of the baseplate could be measured (as indicated in figure 2). Although this configuration does not allow to monitor the temperature of the whole system, given the reduced dimensions of the powder bed it might be taken as representative of the effective thermal history of the build. An alternative solution for the temperature control could be the use of a pyrometer but this equipment has higher capital cost and was therefore not taken into consideration as an option during the realisation of a prototypal system. Future developments of the system could also attempt at using more thermocouples to monitor the temperature along the build direction.

The control of the powder bed temperature was obtained through an ON/OFF solution, whereby the magnetic field was switched on and off. A Zero Voltage Switching (ZVS) circuit was employed to generate the current that was fed to the helical coil to generate the magnetic field. A 48V-20A DC power supply (Mean Well, New Taipei, Taiwan) was employed to power the ZVS circuit. A switch to achieve the ON/OFF control was interposed between the power supply and the ZVS circuit in order to avoid the transient behaviour of the power supply. The resonating frequency of the inductive circuit was estimated as 100 kHz.

2.3. Testing of the high temperature preheating system

The inductive preheating system was tested to 200 °C, 500 °C and 700 °C. The maximum temperature achievable by the inductive preheating system was in excess of 840 °C so the final temperature testing condition which simulated printing conditions and times was conducted at 800 °C. In all tested conditions, the power input to the induction system corresponded to maximum power output of the DC supply which is 960 W. Figure 4(a) shows an incandescent Ti6Al4V substrate during one of the testing phases while figure 4(b) depicts the powder bed at 800 °C during the deposition of a γ-TiAl alloy. Each of the preheating temperature tests consisted of four phases: heating, maintenance, controlled cooling and convective cooling. The heating phase

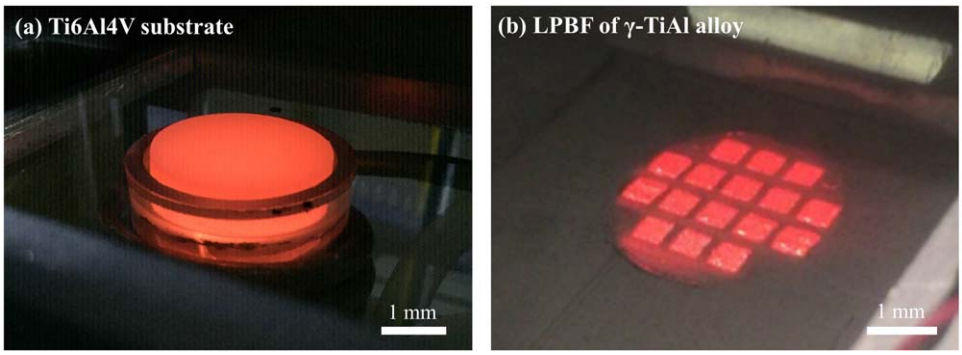

Figure 4. (a) Incandescent Ti6Al4V substrate during the testing of the high temperature induction preheating system and (b) HT-LPBF of a γ-TiAl alloy on project *Grisù*.

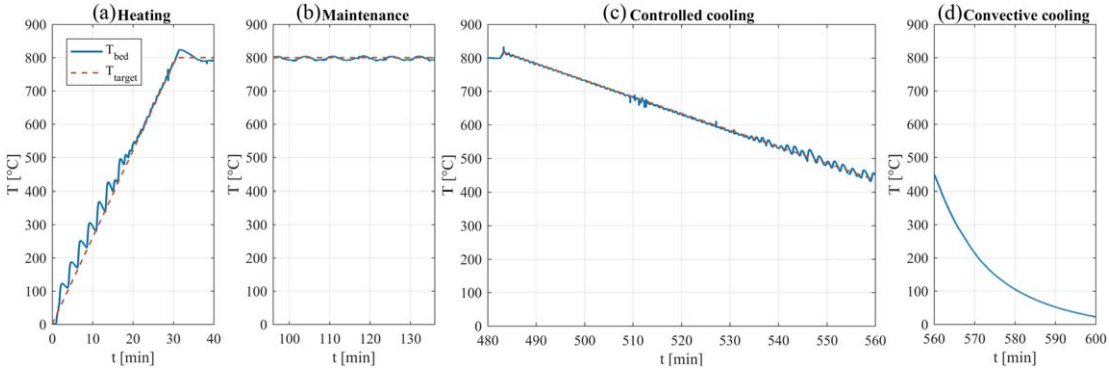

Figure 5. Testing of the inductive preheating system up to 800 °C. Powder bed temperature measured by thermocouple, T_{bed} in blue whilst target temperature, T_{target} when present in orange. Different phases are shown: (a) heating (b) maintenance (c) controlled cooling (d) convective cooling.

must avoid excessive thermal shock on the system components but in any case results less critical since the component of a crack susceptible alloy is yet to be deposited. The time to achieve the operating temperature value of the system was set at 30 min. The maintenance phase at 800 °C was tested for a 450 min duration whereby the temperature oscillated with a $\pm$ 10 °C margin of the target temperature. Finally, the controlled cooling phase is shown, whereby the system was tested to maintain a cooling ratio of 5 °C min^{-1} (always controlled using the ON/OFF control logic previously reported). Finally, a convective cooling of the system was experimented in order to view the behaviour of the system. This was arbitrarily tested from 450 °C downwards.

In figure 5, the temperatures recorded by the thermocouple system are reported during the different phases of the testing at 800 °C (selected time instants are reported). Although, the ON/OFF control introduces an error into the powder bed temperature with respect to the target temperature, this simple control logic system is functional for the aim of the present work. The largest errors with this control logic may be witnessed at temperatures below 500 °C since even if the induction circuit is switched on for a very brief period it rapidly raises the temperature of the system. At higher temperatures, however the error reduces and may be considered as acceptable.

2.4. Processed material

The processability study of γ-TiAl with the novel HT-LPBF system was conducted with a commercially available Ti–48Al–2Cr–2Nb powder (LPW Technology, Runcorn, UK). Scanning electron microscope images of the γ-TiAl powder employed in the current study are visible in figure 6 and show the rounded morphology of the particles.

The chemical composition of the feedstock material as declared by the producer is reported in table 2 while the size distribution parameters are $d_{10} = 16\ \mu$m and $d_{90} = 45\ \mu$m.

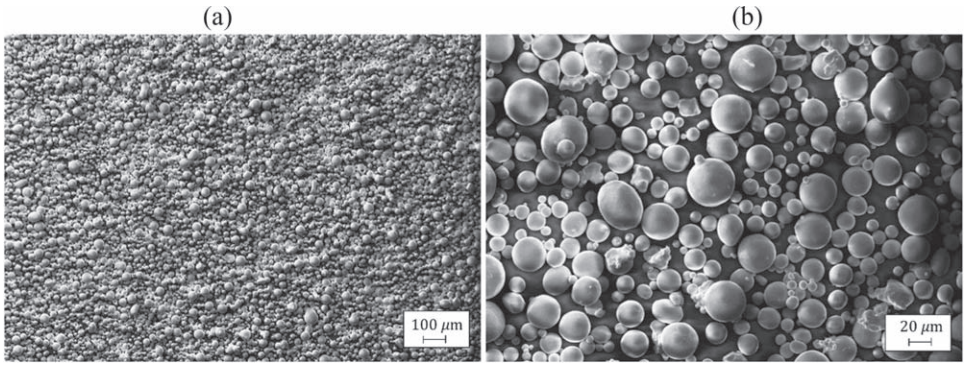

Figure 6. (a) Scanning Electron Microscope images of Ti–48Al–2Cr–2Nb gas atomised powder low magnification and (b) high magnification.

Table 2. Nominal chemical composition of Ti–48Al–2Cr–2Nb.

Element	Ti	Al	Cr	Nb	Fe	Si	C	O	N	H
Wt %	Bal.	34.4	2.58	4.74	0.04	0.006	0.007	0.12	0.006	0.001

2.5. Characterisation

Qualitative evaluation of the top surface and of the polished cross-sections of the specimen deposited was done through optical microscopy images, acquired with a 2.5X objective (Quick Vision ELF from Mitutoyo, Kawasaki, Japan). Where cracking was denoted specimens were evaluated in terms of crack density, ρ_{crack} (mm mm^{-2}) which was calculated as follows:

$$\rho_{crack} = \frac{\sum l_i}{A_{tot}}, \tag{1}$$

whereby l_i is the length of the ith crack being considered, A_{tot} the total area of the specimen and the summation operator is intended for all the cracks present within the considered area. Image analysis of the metallographic cross-sections also allowed to evaluate the apparent density ρ_A (%) of the specimen as:

$$\rho_A = \left(1 - \frac{A_{pore,tot}}{A_{tot}}\right) \cdot 100, \tag{2}$$

where A_{tot} is the total area of the specimen and $A_{pore,tot}$ is the sum of the areas of all pores. Microhardness measurements of the specimen were conducted employing a Leica FM series Vicker hardness measurement system with a 500 g load and 15 s dwell time.

2.6. Experimental plan

LPBF of the Ti–48Al–2Cr–2Nb powder was investigated with and without the use of the high temperature preheating system (i.e. at ambient temperature and with $T_{preheat} = 800$ °C). 4 × 4 mm^2 square hatched laser trajectories were projected on to the powder bed in order to deposit cubic specimen layer-by-layer. Cooling rate of the base plate ($\Delta\dot{T}$) following the LPBF process was controlled when the preheating system was employed and corresponded to 5 °C min^{-1} as suggested by Gussone *et al* [15]. Preliminary investigations indicated the need to use different experimental windows depending if the preheating system was or was not employed (as specified in table 3). The heating cycle depicted in figure 5 was employed during the build with the preheated build. Each experimental condition was replicated twice.

The process results were then evaluated according to the energy density parameter defined as:

$$E_{density} = \frac{P}{vht}, \tag{3}$$

where P is the laser emission power, v the laser scanning speed, h the hatch distance and t the layer thickness. Energy density variations were controlled processing the powder bed with different layer thicknesses whilst the preheating contribution was not taken into account since its contribution is two orders of magnitude lower (i.e. 2 J mm^{-3}).

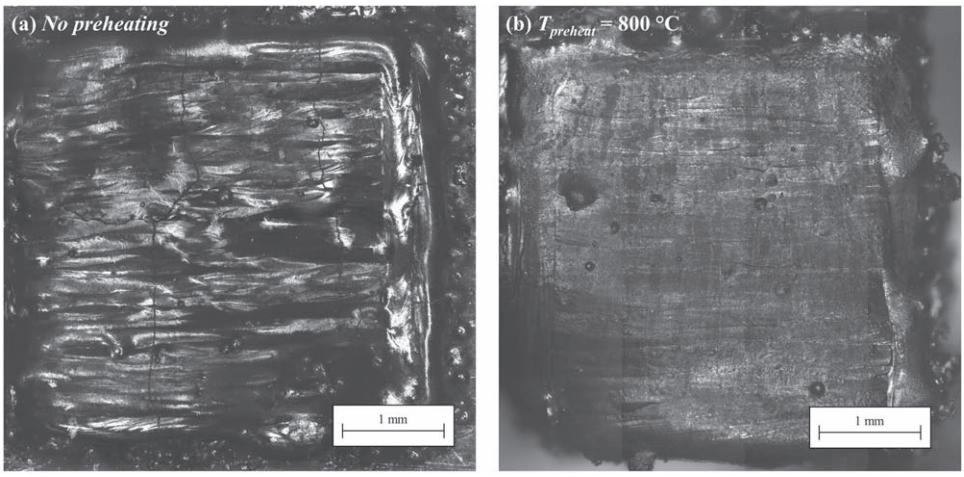

Figure 7. Optical microscope image of the top view of representative specimens (a) no preheating, $P = 150$ W, $v = 200$ mm s^{-1} and (b) with preheating at 800 °C, $P = 150$ W, $v = 200$ mm s^{-1}.

Table 3. Experimental plan specifying fixed and variable process parameters of LPBF of γ-TiAl alloy.

Fixed parameters		
Temperature, $T_{preheat}$ (°C)	None	800
Inert gas	Argon	Argon
Substrate material	Ti6Al4V	Ti6Al4V
Cooling rate, $\Delta\dot{T}$ (°C/min)	Non controlled	5
Hatch distance, h (μm)	70	70
Layer thickness, t (μm)	30	90
Replicates, n	2	2
Variable parameters		
Power, P (W)	150; 200	150; 200
Scan speed, v (mm s^{-1})	100; 150; 200; 250	200; 600; 1000; 1400

3. Results and discussion

In both experimental conditions, with and without the high temperature preheating of the powder bed, it was possible to deposit material onto the Ti6Al4V substrate. However, in the case of the ambient temperature printing of the γ-TiAl alloy, the process had to be interrupted after 10 layers of material had been deposited due to powder bed instabilities and protruding parts which impeded the correct deposition of successive layers. Contrarily, the high temperature preheating at 800 °C was capable of maintaining a stable powder bed and 50 layers were successfully deposited. These instabilities can be clearly viewed from the top surface finish of the specimen realised, shown in figure 7.

Furthermore, it was possible to denote the extensive presence of cracks in the specimens realised at ambient temperature, as evidently shown in the top view of the microscope image of figure 7(a). This was successively confirmed by the observation of the metallographic cross-sections (representative condition shown in figure 8(a)).

Figure 9 reports the measured crack density for the different combinations of process parameters. Results show that it was impossible to realise components by LPBF in γ-TiAl without preheating since the presence of defects highly compromises the structural integrity of the specimens. During the present experimentation, cracking occurred predominantly perpendicular to the scanning direction of the laser beam (as visible in figure 7(a)). This is in agreement with the findings of Löber *et al* whom identified the cracking always perpendicularly to the scanning direction during the single track deposition of a γ-TiAl alloy [24]. Furthermore, the formation of cracks transverse to the advancement of the heat source has been reported for processes anlogous to LPBF (i.e. electron and laser beam welding) [33, 34]. The reason for the formation of such defects can be related to the ductile to brittle transition which occurs around 750 °C and to the strong localised thermal

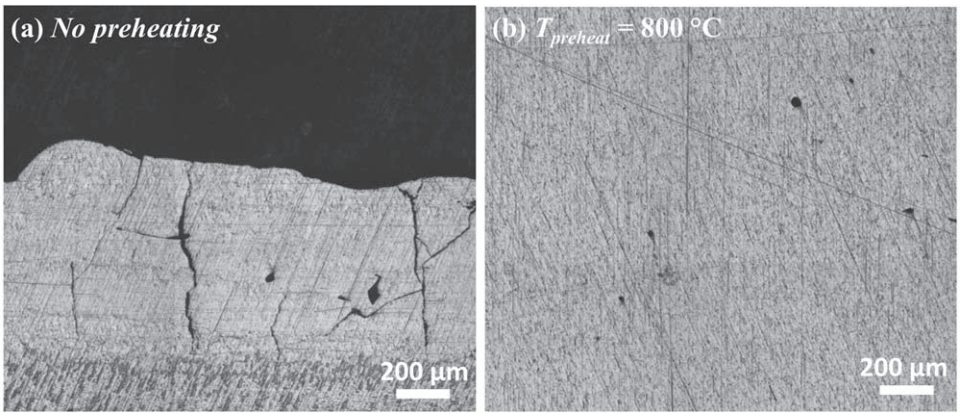

Figure 8. Metallographic cross-sections along build direction of representative specimen (a) no preheating, $P = 150$ W, $v = 200$ mm s^{-1} (b) with $T_{preheat} = 800$ °C, $P = 150$ W, $v = 200$ mm s^{-1}.

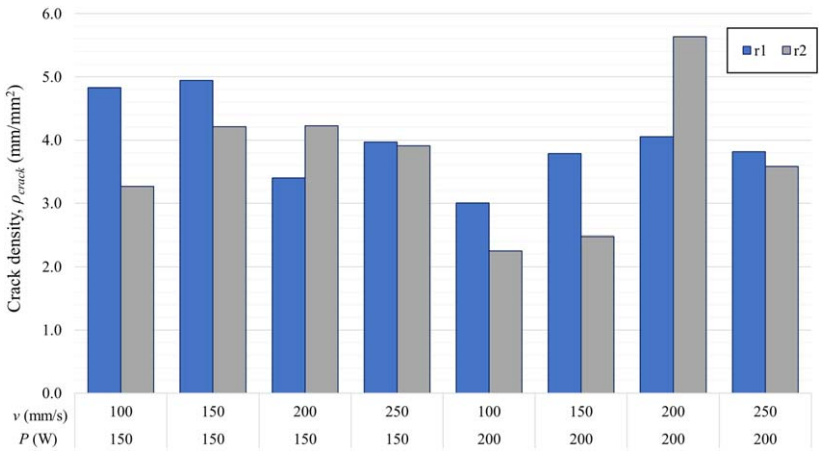

Figure 9. Bar chart reporting the crack density (ρ_{crack}) as a function of process parameters without preheating. Replicates of experimental conditions (r1 and r2) respectively indicated in blue and grey.

stresses generated by the process. γ-TiAl alloys are known to be susceptible to this phenomenon, often referred to as cold cracking [35]. The use of local preheating to minimise thermal stresses has been identified as a solution for the defect-free processing of Titanium–Aluminides [33–35].

On the other hand, in the case of specimens deposited with a preheating temperature of 800°C cracking was not observed in any of the experimental conditions both through the top view microscope images and metallographic cross-sections. Still, the localised presence of rounded pores may be viewed in figure 8(b). Accordingly, the morphology of these pores indicates that gas entrapment during the rapid solidification is accountable for their formation [36, 37]. The absence of cracks in the cross-section of the specimens deposited with high temperature preheating confirms results coming from previous literature studies and shows promising results for the development of industrial systems capable of realising fully functional γ-TiAl components. In order to establish optimal processing parameters, the apparent density of the specimens deposited with the high temperature preheating has been plotted against the process energy density (results shown in figure 10). It is possible to observe how the material processed using this system presents the typical behaviour of commonly deposited materials such as Ti6Al4V and AISI 316L [38, 39], where a high porosity processability region may be found at low levels of energy density followed by a high apparent density region as the energetic input is increased. At low energy densities the process generates lack of fusion defects as may be inferred from the jagged and irregular shape of the pores [40]. It is possible to view from the data and cross-sections reported in figure 10, that as the energy density is increased the porosity reduced until apparent densities in excess of 99% are achieved. An excessive energy input process region was not determined but experimentation at higher levels of energy density will probably yield greater porosity caused by gas entrapment due to the keyhole formation. This type of defect formation at elevated energy densities levels has been previously denoted by Cunnigham *et al* [40] through x-ray microtomographies and by Martin *et al* [41] by means of high speed synchrotron x-ray imaging.

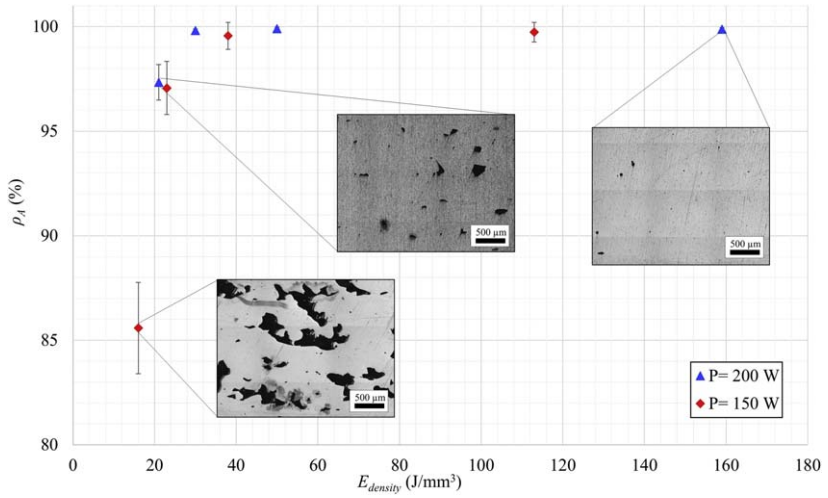

Figure 10. Apparent density ρ_A of the specimens deposited with preheating temperature $T = 800°C$ against energy density $E_{density}$ delivered during the process. Error bars refer to the 95% confidence interval. Metallographic cross-sections of specific conditions are shown.

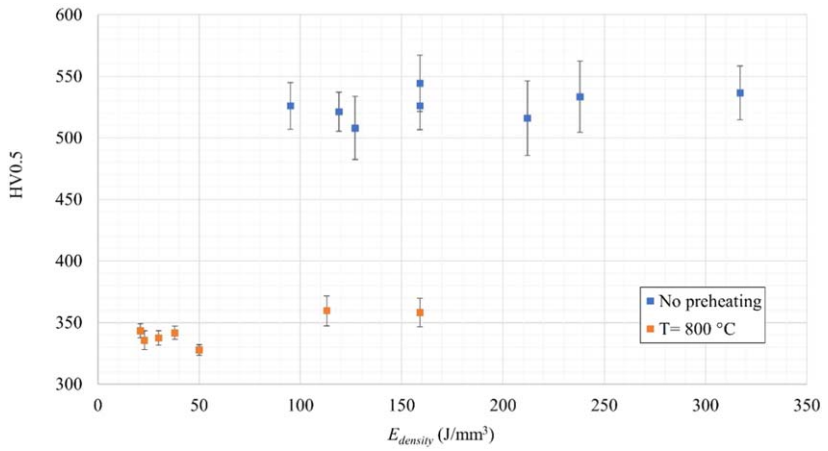

Figure 11. Microhardness results as a function of energy density. No preheating results in blue, with preheating at $T = 800$ °C in orange. Error bars indicate 95% confidence interval.

Microhardness measurements are reported in figure 11 as a function of energy density. However, in this case it is not possible to determine a trend of the material properties in terms of this indicator. The difference between processing conditions is dictated by the starting temperature of the powder bed, as may be viewed by the different clusters of figure 11. The deposition done without the inductive preheating report significantly higher values of microhardness comparable to the results reported by Vilaro *et al* and Li *et al* for the processing of intermetallic γ-TiAl alloys [23, 42]. On the other hand, the microhardness of specimens deposited at $T_{preheat} = 800$ °C is similar to the values obtained by Murr *et al* during the EBM of Ti–47Al–2Nb–2Cr powder [18]. As a matter of fact, the high temperature preheating and slower cooling rate is expected to prevent the formation of localised α_2 phase and rather enable the formation of γ/α_2 lamellar crystalline clusters which have a higher ductility and avoid cold cracking. Thus this may also explain the difference in hardness values between the samples realised with or without preheating [15, 34]. This is a further indicator of a stable and successful process outcome with the novel LPBF system developed indicating its potential for the direct fabrication of γ-TiAl components.

4. Conclusions

The main objective of the present work, namely the realisation of a novel HT-LPBF system capable of processing γ-TiAl was achieved. Project *Grisù* was successfully tested to preheat the powder bed up to 800 °C. A demonstrator print of Ti–48Al–2Cr–2Nb was conducted both with and without preheating in order to verify the

functionality of the system in processing crack susceptible alloys. The temperature control implemented maintained successfully the temperature within the desired range and allowed control over the cooling rate of the build, preventing crack formation of the deposited samples. Specimens processed without the use of the inductive system presented severe cracks with cracking densities always in excess of 3 mm mm^{-2}. The defects developed perpendicularly to the scanning direction of the laser beam and are related to the cold cracking formation mechanism. On the other hand, components realised at $T_{preheat} = 800\,^{\circ}$C, did not show the presence of cracks under optical microscope inspection.

Porosity could be reduced by regulating the laser process parameters through the energy density indicator, achieving values in excess of 99.5% for $E_{density} > 30$ J mm^{-3}. Microhardness in the order of 350 HV were obtained with $T_{preheat} = 800\,^{\circ}$C. Whilst the excessive thermal gradients and cooling rates due to the laser processing of the material without the use of the preheating system, yielded hardness values in above 500 HV which indicate a more brittle microstructure. Future work on the prototypal system will investigate in detail the laser-powder interaction area with diagnosis equipment and characterise further the material properties.

Acknowledgments

The authors wish to express their gratitude to Dr Eligio Grossi for his contribution in the design of the prototype system and in the preliminary testing and experiment execution. Acknowledgments go also to Optoprim for providing the controller system and scanner head and to n-Light for the laser source. This work was supported by European Union, Repubblica Italiana, Regione Lombardia and FESR through the project MADE4LO under the call 'POR FESR 2014-2020 ASSE I - AZIONE I.1.B.1.3'.

ORCID iDs

Leonardo Caprio https://orcid.org/0000-0003-4964-9698
Ali Gökhan Demir https://orcid.org/0000-0002-8000-468X
Barbara Previtali https://orcid.org/0000-0002-6074-8753

References

[1] Demir A G, Colombo P and Previtali B 2017 From pulsed to continuous wave emission in SLM with contemporary fiber laser sources: effect of temporal and spatial pulse overlap in part quality *Int. J. Adv. Manuf. Technol.* **91** 2701–14
[2] Scipioni Bertoli U, Guss G, Wu S, Matthews M J and Schoenung J M 2017 *In situ* characterization of laser-powder interaction and cooling rates through high-speed imaging of powder bed fusion additive manufacturing *Mater. Des.* **135** 385–96
[3] Shi Q, Gu D, Xia M, Cao S and Rong T 2016 Effects of laser processing parameters on thermal behavior and melting/solidification mechanism during selective laser melting of TiC/Inconel 718 composites *Opt. Laser Technol.* **84** 9–22
[4] Hagedorn Y, Risse J, Meiners W, Pirch N, Wissenbachand K and Poprawe R 2013 Processing of nickel based superalloy MAR M-247 by means of High-Temperature Selective Laser Melting (HT-SLT) *Proc. 6th Int. Conf. Adv Res Virtual Rapid Prototyp* pp 291–5
[5] Agarwala M, Bourell D, Beaman J, Marcus H and Barlow J 1995 Direct selective laser sintering of metals *Rapid Prototyping J.* **1** 26–36
[6] Das S, McWilliam J, Wu B and Beaman J J 1991 Design of a high temperature workstation for the selective laser sintering process *1991 Int. Solid Freeform Fabrication Symp.*
[7] McWilliams J, Hysinger C and Beaman J J 1992 Design of a high temperature process chamber for the selective laser sintering process *1992 Int. Solid Freeform Fabrication Symp.*
[8] Aboulkhair N T, Everitt N M, Ashcroft I and Tuck C 2014 Reducing porosity in AlSi10Mg parts processed by selective laser melting *Additive Manuf.* **1** 77–86
[9] Demir A G and Previtali B 2017 Investigation of remelting and preheating in SLM of 18Ni300 maraging steel as corrective and preventive measures for porosity reduction *Int. J. Adv. Manuf. Technol.* **93** 2697–709
[10] Colopi M, Demir A G, Caprio L and Previtali B 2019 Limits and solutions in processing pure Cu via selective laser melting using a high-power single-mode fiber laser *Int. J. Adv. Manuf. Technol.* **2019** 1–14
[11] Wilkes J, Hagedorn Y, Meiners W and Wissenbach K 2013 Additive manufacturing of ZrO_2–Al_2O_3 ceramic components by selective laser melting *Rapid Prototyping J.* **19** 51–7
[12] Kempen K, Vrancken B, Buls S, Thijs L, Van Humbeeck J and Kruth J-P 2014 Selective laser melting of crack-free high density M2 high speed steel parts by baseplate preheating *J. Manuf. Sci. Eng.* **136** 061026
[13] Ali H, Ma L, Ghadbeigi H and Mumtaz K 2017 *In situ* residual stress reduction, martensitic decomposition and mechanical properties enhancement through high temperature powder bed pre-heating of selective laser melted Ti6Al4V *Mater. Sci. Eng.* A **695** 211–20
[14] Gussone J *et al* 2017 Microstructure stability of γ-TiAl produced by selective laser melting *Scr. Mater.* **130** 110–3
[15] Gussone J, Hagedorn Y C, Gherekhloo H, Kasperovich G, Merzouk T and Hausmann J 2015 Microstructure of γ-titanium aluminide processed by selected laser melting at elevated temperatures *Intermetallics* **66** 133–40
[16] Mertens R, Dadbakhsh S, Van Humbeeck J and Kruth J P 2018 Application of base plate preheating during selective laser melting *Proc. CIRP.* **74** 5–11
[17] Aggarangsi P and Beuth J L 2006 Localized preheating approaches for reducing residual stress in additive manufacturing *Proc SFF Symp (Austin.)* pp 709–20
[18] Murr L E *et al* 2010 Characterization of titanium aluminide alloy components fabricated by additive manufacturing using electron beam melting *Acta Mater.* **58** 1887–94

[19] Caprio L, Chiari G, Demir A G and Previtali B 2018 Development of novel high temperature laser powder bed fusion system for the processing of crack-susceptible alloys *Solid Free Fabr 2018 Proc. 29th Annu Int. Solid Free Fabr Symp—An Addit Manuf Conf.* pp 2275–85
[20] Clemens H, Wallgram W, Kremmer S, Güther V, Otto A and Bartels A 2008 Design of novel β-solidifying TiAl alloys with adjustable β/B2-phase fraction and excellent hot-workability *Adv. Eng. Mater.* **10** 707–13
[21] Liu Y J *et al* 2016 Microstructure, defects and mechanical behavior of beta-type titanium porous structures manufactured by electron beam melting and selective laser melting *Acta Mater.* **113** 56–67
[22] Biamino S *et al* 2011 Electron beam melting of Ti–48Al–2Cr–2Nb alloy: microstructure and mechanical properties investigation *Intermetallics* **19** 776–81
[23] Vilaro T *et al* 2010 Direct fabrication of a Ti–47Al–2Cr–2Nb alloy by selective laser melting and direct metal deposition processes *Adv. Mater. Res.* **89–91** 586–91
[24] Löber L, Schimansky F P, Kühn U, Pyczak F and Eckert J 2014 Selective laser melting of a beta-solidifying TNM-B1 titanium aluminide alloy *J. Mater. Process. Technol.* **214** 1852–60
[25] Doubenskaia M, Domashenkov A, Smurov I and Petrovskiy P 2018 Study of selective laser melting of intermetallic TiAl powder using integral analysis *Int. J. Mach. Tools Manuf.* **129** 1–14
[26] Li W *et al* 2016 Effect of substrate preheating on the texture, phase and nanohardness of a Ti–45Al–2Cr–5Nb alloy processed by selective laser melting *Scr. Mater.* **118** 13–8
[27] Li W *et al* 2017 Enhanced nanohardness and new insights into texture evolution and phase transformation of TiAl/TiB2 *in situ* metal matrix composites prepared via selective laser melting *Acta Mater.* **136** 90–104
[28] Li M *et al* 2018 TiAl/RGO (reduced graphene oxide) bulk composites with refined microstructure and enhanced nanohardness fabricated by selective laser melting (SLM) *Mater. Charact.* **143** 197–205
[29] Li W *et al* 2018 Enhanced compressive strength and tailored microstructure of selective laser melted Ti–46.5Al–2.5Cr–2Nb–0.5Y alloy with different boron addition *Mater. Sci. Eng.* A **731** 209–19
[30] Ma C, Gu D, Dai D, Zhang H, Du L and Zhang H 2018 Development of interfacial stress during selective laser melting of TiC reinforced TiAl composites: influence of geometric feature of reinforcement *Mater. Des.* **157** 1–11
[31] Demir A G, Monguzzi L and Previtali B 2017 Selective laser melting of pure Zn with high density for biodegradable implant manufacturing *Additive Manuf.* **15** 20–8
[32] Rudnev V, Loveless D and Cook R L 2017 *Handbook of Induction Heating* 2nd edn (Boca Raton, FL: CRC Press)
[33] Liu J, Dahmen M, Ventzke V, Kashaev N and Poprawe R 2013 The effect of heat treatment on crack control and grain refinement in laser beam welded beta-solidifying TiAl-based alloy *Intermetallics* **40** 65–70
[34] Chen G, Zhang B, Liu W and Feng J 2011 Crack formation and control upon the electron beam welding of TiAl-based alloys *Intermetallics* **19** 1857–63
[35] Leyens C and Peters M 2003 *Titanium and Titanium Alloys: Fundamentals and Applications* ed J W Sons (New York: Wiley)
[36] Panwisawas C, Qiu C L, Sovani Y, Brooks J W, Attallah M M and Basoalto H C 2015 On the role of thermal fluid dynamics into the evolution of porosity during selective laser melting *Scr. Mater.* **105** 14–7
[37] Khairallah S A, Anderson A T, Rubenchik A and King W E 2016 Laser powder-bed fusion additive manufacturing: physics of complex melt flow and formation mechanisms of pores, spatter, and denudation zones *Acta Mater.* **108** 36–45
[38] Gong H, Rafi K, Gu H, Starr T and Stucker B 2014 Analysis of defect generation in Ti–6Al–4V parts made using powder bed fusion additive manufacturing processes *Additive Manuf.* **1** 87–98
[39] Kamath C, El-Dasher B, Gallegos G F, King W E and Sisto A 2014 Density of additively-manufactured, 316L SS parts using laser powder-bed fusion at powers up to 400 W *Int. J. Adv. Manuf. Technol.* **74** 65–78
[40] Cunningham R, Narra S P, Montgomery C, Beuth J and Rollett A D 2017 Synchrotron-based x-ray microtomography characterization of the effect of processing variables on porosity formation in laser power-bed additive manufacturing of Ti–6Al–4V *JOM* **69** 479–84
[41] Martin A A *et al* 2019 Dynamics of pore formation during laser powder bed fusion additive manufacturing *Nat. Commun.* **10** 1–10
[42] Li W, Liu J, Wen S, Wei Q, Yan C and Shi Y 2016 Crystal orientation, crystallographic texture and phase evolution in the Ti–45Al–2Cr–5Nb alloy processed by selective laser melting *Mater. Charact.* **113** 125–33